Hierarchical Packing Model: Estimating the Overall Particle Size Distribution from Surface Images and Permeability Properties

Jinshi Liu, Zhaohui Jiang, *Member, IEEE*, Weihua Gui, *Member, IEEE*, Zhiwen Chen, *Member, IEEE*, Weichao Luo, *Member, IEEE*, and Chaobo Zhang, *Member, IEEE*

***Abstract*—Determining the particle size distribution (PSD) of an industrial particle stack with precision is imperative. The inherent challenge arises from the concealed distribution within the stack. In response, we introduce a comprehensive framework that extrapolates the overall PSD from the observable surface images of the particle stack. Our methodology initiates by characterizing the hierarchical structure of the particle stack, grounded in its formation mechanism, effectively demarcating between surface and internal information. Subsequently, we present the Hierarchical Packing Model (HPM), an innovation that integrates the permeability principle, spatial structural attributes, and a stochastic resampling probability paradigm specific to particle stacks. This model crystallizes a quantitative nexus between the surface and overall PSD of the particle stack. As an integral component, we deploy a fine-tuned segmentation large model to extract particle boundaries within the surface imagery, facilitating a statistical assessment of the surface PSD. This value can then be substituted into the HPM to obtain the overall PSD. To underscore the robustness and precision of our methodology, we executed comparative and ablation studies utilizing datasets from a blast furnace ironmaking facility. The empirical outcomes unequivocally attest to the precision and effectiveness of our method.**

***Index Terms*—Particle size distribution, Particle Permeability, Image Segmentation, Random Resampling, Packing Density.**

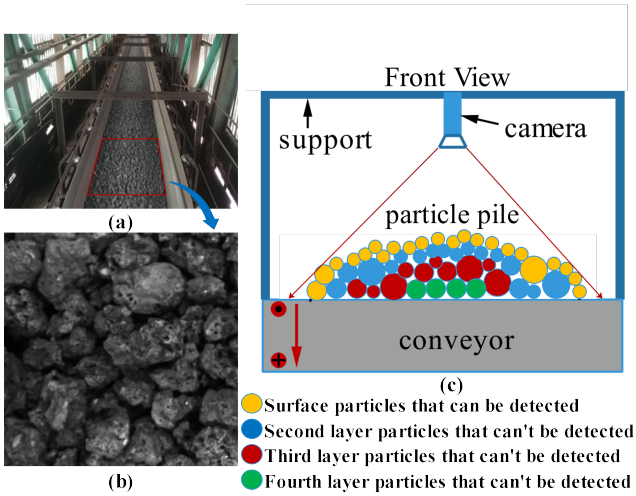

Figure 1. Detecting a particle stack on a conveyor by a visual perception method, such as an industrial camera only acquires information about its surface. (a) particle stacks on conveyor belts; (b) the particle stack surface images captured by an industrial camera; (c) Hierarchical structure of the collected particle stacks.

I. INTRODUCTION

PARTICLE size distribution (PSD) is an essential parameter that reflects the porosity, structure, and packing density of a particulate system [1]–[4]. Its importance is underscored by its profound implications across a myriad of industrial sectors. For instance, within the realm of ironmaking, the blast furnace (BF) stands as the central apparatus [5]–[8]. Here, the material's PSD directly mirrors the performance of the charging system. As such, guaranteeing the precision and consistency of PSD measurements is paramount for managing gas permeability and ensuring the furnace's internal reaction stability. In a similar vein, during mineral processing, PSD becomes pivotal for the selection of valuable minerals [9]. Hence, developing an accurate online estimation method for PSD is of great value for many industrial applications.

Numerous methodologies exist for assessing PSD, each necessitating distinct instruments. These instruments, intrinsic to their respective measurement techniques, exhibit diverse characteristics. Through our extensive investigation, we have stratified the prevailing methodologies for PSD measurement into three principal categories: simple equipment methods, precision instrument methods, and imaging analysis methods.

Simple Equipment Methods: This classification includes methods that leverage fundamental physical attributes, utilizing straightforward apparatus such as sieves. While these methods provide rapid and economical assessments, they tend to sacrifice a degree of precision.

Precision Instrument Methods: Exploiting sophisticated physical principles such as light scattering, laser phase Doppler, and aerodynamics, these methods depend on state-

This work was supported by the National Major Scientific Research Equipment of China (No. 61927803) and the Central South University Post-Graduate Independent Exploration and Innovation Project under Grant 2023zzts0619. (Corresponding author: Zhaohui Jiang).

Jinshi Liu, Zhaohui Jiang, Weihua Gui, and Zhiwen Chen are with the School of Automation, Central South University, Changsha 410083, China. Weihua Gui, Weichao Luo, and Chaobo Zhang are with the Pengcheng Laboratory, Shenzhen 518055, China. (e-mail: ljs11528@csu.edu.cn; jzh0903@csu.edu.cn; gwh@csu.edu.cn; zhiwen.chen@csu.edu.cn; luowch@pcl.ac.cn; zhangchb@pcl.ac.cn.)

of-the-art instruments and are predominantly designed for offline sampling. Despite their exceptional precision, real-time measurements remain elusive. Light scattering stands out within this bracket, offering particle size insights by assessing the scattered light signals produced when particles interact with light sources [10]. With a measurement spectrum ranging from 0.1 to 25 mm, it assures swift, consistent, and accurate results, albeit with the prerequisites of regular calibration and offline sampling. Leveraging the Mie scattering paradigm, the laser phase Doppler technique gauges particle size, effective in a range between 1.0E-06 to 1.0E-03 mm [11]. Its robustness against environmental factors such as temperature and pressure is noteworthy. However, its limitation to single-point measurements and dependence on offline sampling are discernible constraints. Conversely, the aerodynamic approach determines particle size by capitalizing on the distinct accelerations generated by differently sized particles in a quickened airflow [12]. Encompassing a measurement range of 0.37 to 20 mm, this technique remains unswayed by the refractive indices or densities of particles. Nevertheless, potential pitfalls include interference from overlapping particles and, again, the requisite offline sampling. In summary, while these methods each offer unique strengths, their shared constraints of offline sampling and limited size range coverage make it a challenge to cater to demands for both high-speed and high-precision detection.

Imaging Analysis Methods: This category embraces methods that utilize digital image techniques, including traditional segmentation, semantic segmentation, instance segmentation, and object detection, to analyze surface images procured from imaging apparatuses such as cameras. Distinctively, they achieve real-time assessments with commendable accuracy, though their outcome remains a surface PSD. Given this context, the majority of academic endeavors are channeled towards augmenting the efficacy of segmentation models directly at the algorithmic level [4], [15]. Several initiatives prioritize semantic segmentation models, aiming to extract richer feature sets. Illustratively, Wang et al. introduced an evolved VGGNet tailored for coal dust image feature extraction [16]. Singh et al. employed UNet for segmenting river ice imagery and discerning ice particles, paralleled by Liu et al.'s innovative strategy for industrial chip metric identification anchored in cascaded region segmentation tailored for surface-mount devices [17], [18]. Conversely, some scholars pivot towards instance segmentation models, aiming to refine the integrity of particle contour detection [19], [20]. Still others gravitate towards object detection models, seeking to pinpoint particle position and morphology [21]–[23]. Notwithstanding their merits, it's pivotal to recognize that these primarily yield surface PSD, as depicted in Fig. 1.

While imaging analysis methods, in their present state, fall short of directly gauging the overall PSD, we present an innovative remedy within this manuscript. We propose the Hierarchical Packing Model (HPM), a mathematical model mindful of the spatial alignment and formation mechanism of particle stacks. Drawing on particle layering nuances and stochastic sampling, the HPM forges a nexus between surface and overall PSDs. The surface PSD, ascertained via the segmentation model, becomes the linchpin for deducing the overall PSD. The groundbreaking contributions of this manuscript encapsulate:

(1) This paper proposes an algorithmic framework to estimate overall PSD based on surface images and permeability characteristics of particle stacks.

(2) The packing density is used to derive an analytical expression for particle permeability, which quantifies the particle stack formation process and enables analysis of the overall PSD.

(3) We quantitatively describe the relationship between surface PSD and overall PSD using an HPM derived from the permeability principle, spatial distribution, and random resampling of particle stacks.

II. METHODOLOGY

A. Motivation

Our primary aim is to derive a mathematical relationship between the surface and overall PSD, focusing on the intricate process of particle stack formation. We conceptualize this formation process as a series of random samplings, viewing each particle as an individual entity. From the standpoint of inter-particle dynamics, the stacking eventuates when smaller particles infiltrate the voids. Moreover, overarching spatial distribution patterns play a pivotal role in this dynamic. Armed with these insights, we've crafted a model encapsulating random sampling, particle infiltration, and spatial distribution elements. This model aims to unravel the intricate ties between the surface and overall PSD. To materialize our objectives, we deploy the meticulously calibrated SAM segmentation model [14], enabling us to isolate particle contours from the surface image and, consequently, deduce the surface PSD. The finale of our approach involves integrating the extracted surface PSD into our proposed model, thereby calculating the overall PSD, as illustrated in Fig. 2.

B. Hierarchical Packing Model

Imagine the particle stacking process as akin to assembling building blocks, one layer upon another. This process gives rise to a particle stack characterized by distinctive spatial stratification properties. The cross-section of the particle stack can be divided into H discrete layers.

The topmost layer that can be directly detected is noted as the first layer. Then, each particle size interval is denoted by $[(n-1)\times s_0, n\times s_0)$ $(n \in \mathbb{N})$, where s_0 represents the interval width. The number of intervals is denoted by k, and we have $s_0 \times k = Y$, where Y is a constant. Based on the average size of test particles, we have set Y to 80 mm. To create a PSD, we can set different numbers of intervals k, usually 4, 8, or 10, and adjust the interval width s_0 accordingly.

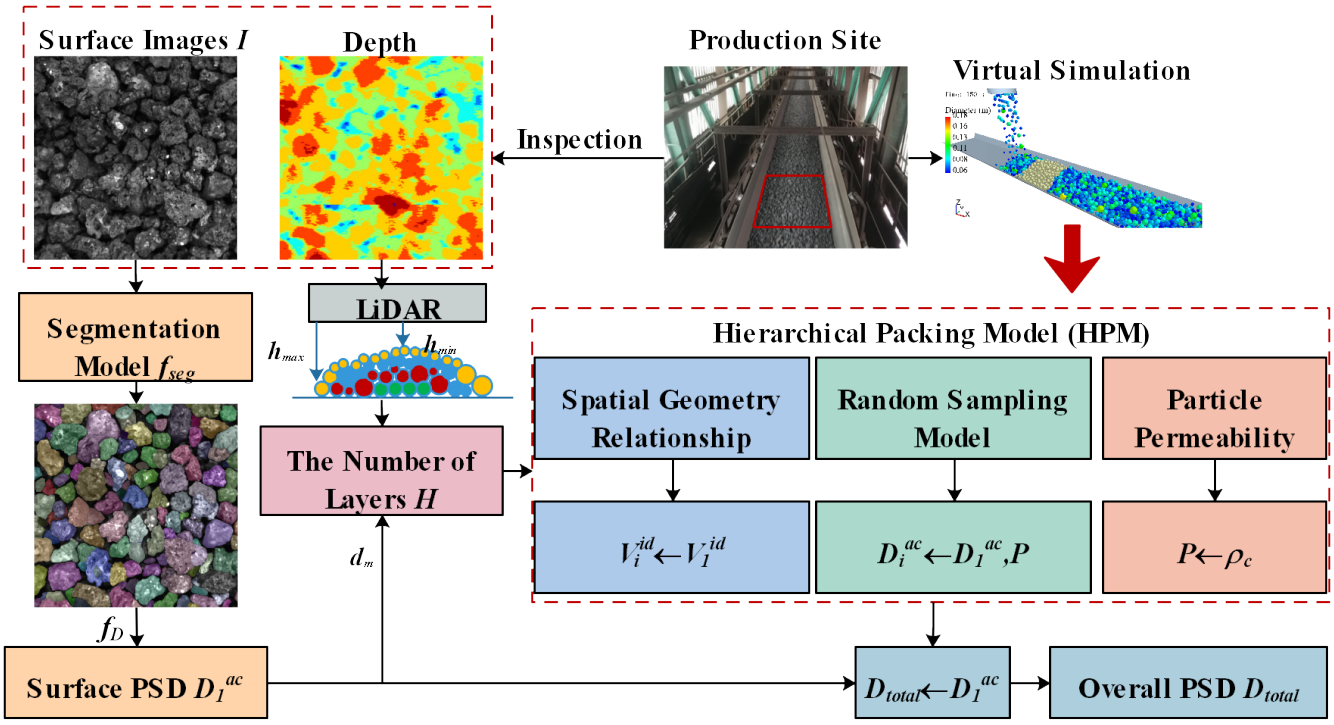

Figure 2. The structure of the proposed framework. f_D indicates a single particle size calculation method. V_i^{id} indicates the particle stack volume in the i-th layer under ideal stratification. D_i^{ac} indicates the PSD for the i-th layer under actual stratification. ρ_c indicates the packing density of particle stacks.

For example, if k=4, the PSD is a 4-dimensional vector with values for each dimension representing the number of particles in [0,20], [20,40], [40,60], and [60,80]. With k=8, the particle intervals are [0,10], [10,20], ... [60,70], and [70,80]. For k=10, the particle intervals are [0,8], [8,16],..., [64,72], and [72,80]. In summary, the particle stack overall PSD can be defined as:

$$D_{total} = \sum_{i=1}^{H} D_i^{ac} = [\sum_{i=1}^{H} N_{i,1}, \sum_{i=1}^{H} N_{i,2}, ..., \sum_{i=1}^{H} N_{i,k}] \quad (1)$$

where D_i^{ac} denotes the actual PSD for i-th layer, D_{total} indicates the actual overall PSD, $N_{i,k}$ indicates the number of particles in the k-th particle level interval, and i represents the particles in the i-th layer.

1) Particle Permeability Relationship: While surface detection methods grounded in visual perception can effectively compute the surface PSD, directly calculating the PSD in other layers is infeasible. Our inspiration stems from the literature [24], [25], which posits that minute particles have a propensity to pass through inter-particle gaps in lower layers and accumulate during their journey. Smaller particles can readily infiltrate the lower layer through these gaps. As resistance mounts, this penetration becomes progressively more challenging. Therefore, to streamline the calculation process, we opt to consider only the infiltration of the current layer into the subsequent layer, disregarding deeper-layer infiltration as its probability is minimal and negligible. By adhering to this rationale, we can establish a clear relationship between the PSDs of each individual layer.

$$D_i^{ac} = D_i^{id} + \left\lceil \frac{i-1}{i} \right\rceil D_{i-1}^{id} * P_{i-1} - \left\lceil \frac{H-i}{H} \right\rceil D_i^{id} * P_i \quad (2)$$

where D_i^{id} indicates the ideal PSD for the i-th layer without considering particle permeability, and $P_i = [p_{i,1}, p_{i,2}, \ldots, p_{i,k}]$ denotes the probability that particles in the former layer penetrates into the void in the lower layer, called the particle permeability. Both P_i and D_i can be viewed as $1 \times k$ matrices, and $*$ denotes element-wise multiplication, also known as Hadamard Product [26].

2) Spatial Geometry Relationship: Determining the PSD for each individual layer is undeniably intricate. However, by approximating each particle as a uniform sphere, we can forge a direct, quantitative link between particle size and its volume. This analogy allows us to envision the particle stack's spatial structure as a composite of multiple cylindrical forms. To determine the number of layers H in the particle stack, based on its ideal spatial distribution, we can employ the formula $H = \left\lfloor \frac{h_{max}-h_{min}+d_m}{d_m} \right\rfloor$, where h_{max} and h_{min} represent the maximum and minimum depth in the surface image, respectively. Generally, depth information is obtained via laser inspection, and d_m denotes the average particle diameter. The ideal spatial distribution of a particle stack with a three-layer structure is shown in

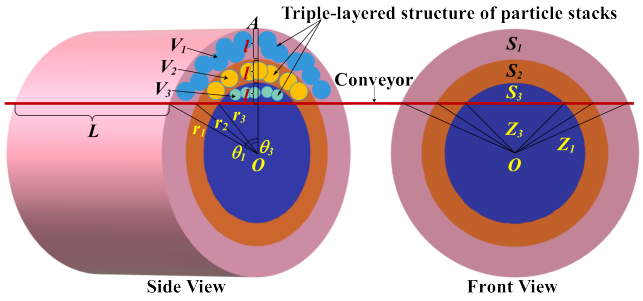

Figure 3. An ideal geometric model of a particle stack.

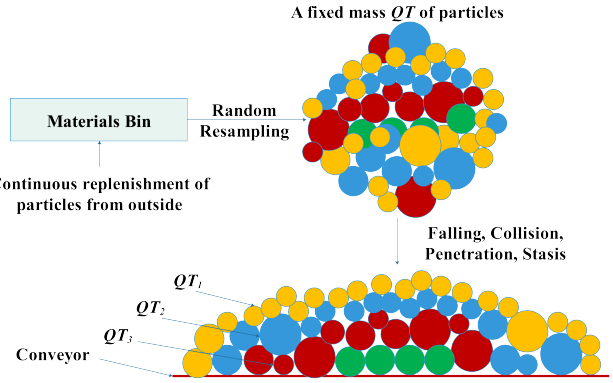

Figure 4. The process of random resampling of particles from a silo.

Fig. 3.

$$\begin{aligned} V_3^{id} &= L\left[\frac{1}{2}r_3^2 \arg\cos\varphi_3 - (r_3-l)\sqrt{r_3^2-(r_3-l)^2}\right] \\ &= LS_3 = L(F_3 - Z_3) \\ V_2^{id} &= LS_2 = L(F_2 - S_3 - Z_2) \\ V_1^{id} &= LS_1 = L(F_1 - S_2 - S_3 - Z_1) \end{aligned} \tag{3}$$

where $\varphi_i = \cos 2\theta_i = \frac{2(r_i-l)^2 - r_i^2}{r_i^2}$ denotes the cosine of $2\theta_i$ (twice the angle formed by r_i and AO), and $r_i = r_3 + (3-i)l$. In this paper, L denotes the imaging length of the camera on the conveyor belt, Z denotes the isosceles triangle area in the front view, V^{id} indicates the particle stack ideal volumes under loose accumulation, and S denotes the cross-sectional area for each layer. Therefore, we can express the ideal volume relationship for each layer as

$$V_i^{id} = \frac{S_i}{S_1} V_1^{id} \tag{4}$$

3) Random Resampling Model: Yet, even with a grasp of the ideal volume for each layer, bridging this understanding to the PSD is not straightforward. Dispensing particles from a storage bin emerges as an inherently unpredictable procedure, especially when overlooking particle permeability during stacking. Given this unpredictability, we propose a statistical and probabilistic model to decipher the optimal PSD for each layer. Envision a scenario: particles, varying in size, continuously tumble out of the bin onto a conveyor due to gravitational forces. This flow of particles can be likened to a random sampling event. From a probabilistic standpoint, the bin is akin to a container teeming with balls of assorted dimensions. When particles are released from the bin at a steady rate, it mirrors the act of randomly selecting certain balls based on a set criterion, where the volume sampled at any instant remains constant. Since the bin is consistently replenished with the same type of particles from the outside in the same batch, it is a put-back sampling (where the number and average size of particles in the silo remain unchanged), as depicted in Fig. 4.

$$Q = \frac{V_i^{id}\rho_p}{T_i} = \frac{\rho_p}{T_i}\sum_{j=1}^{N_i} v_j = \frac{\pi\rho_p}{6T_i}\left(\sum_{j=1}^{N_i} d_j^3\right) = \frac{\pi\rho_p}{6T_i}\left(\sum_{q=1}^{k}\sum_{p=1}^{n_{i,q}} d_p^3\right) \tag{5}$$

where $D_i^{id} = [n_{i,1}, n_{i,2}, ..., n_{i,k}]$ and $N_i = \sum_{j=1}^{k} n_{i,j}$. In this paper, ρ_p indicates the particle density, Q denotes the mass flow rate, and $n_{i,q}$ denotes the number of particles in the q-particle interval in the i-th layer. T_i represents the ideal time taken to remove all the particles in layer i from the bin, d_j indicates the diameter of the j-th particle, and v_j denotes the volume of the j-th particle. From the above equation, it is obviously easy to know that

$$n_{i,1}, n_{i,2}, \cdots, n_{i,k} \propto V_i^{id} \tag{6}$$

Then, in connection with the ideal volume relation Eq. 4 derived in the previous section, we can obtain

$$D_i^{id} = \frac{S_i}{S_1} D_1^{id} \tag{7}$$

Subsequently, according to the formula Eq. 2, we can get

$$D_i^{id} = \frac{S_i}{S_1} D_1^{id} = \frac{S_i}{S_1} D_1^{ac} * f_{rec}(O - P_1) \tag{8}$$

where O indicates a $1 \times k$ one-matrix, and f_{rec} denotes the reciprocal operation. Next the Eq. 2 is summed in H terms and then we get

$$\sum_{i=1}^{H} D_i^{ac} = \sum_{i=1}^{H} D_i^{id} = \sum_{i=1}^{H} \frac{S_i}{S_1} D_1^{ac} * f_{rec}(O - P_1) \tag{9}$$

At this point, the only unknowns in Eq. are D_1^{ac} and P_1. We will calculate D_1^{ac} using a visual perception-based detection method. The packing density is used to calculate P_1.

4) Particle Permeability from Packing Density: Understanding particle permeability is conceptually anchored in earlier research on packing density, which is defined as the ratio of the particle volume to the overall volume of the particle stack.

$$\rho = \frac{V_p}{V} = \frac{V_p}{V_p + V_\varphi} \tag{10}$$

where ρ indicates the packing density, V_p denotes the volume of particles, and V_φ represents the volume of voids. The conundrum of packing density has its roots in the 17th century, first introduced by Kepler. He postulated a scenario

concerning the optimal arrangement of identical spheres to maximize packing density. Kepler's hypothesis suggested two possible configurations for the highest achievable packing density: face-centered cubic (FCC) and hexagonal close packing (HCP) [**?**], [27], [28]. Over the ensuing centuries, numerous experiments have been conducted to delve into this hypothesis. One consistent observation has emerged: regardless of the size, the packing density for an individual sphere remains constant, a fact visually represented in Fig. 5. There are three repeatable stacking forms: (1) random loose packing (RLP) with a packing density of $\rho \leq 0.60$ when particles are poured gently into a container, (2) random close packing (RCP) with a packing density of approximately $\rho \approx 0.64$ when subjected to various forms of vibration, and (3) ordered close packing (OCP) with a packing density of approximately $\rho \approx 0.74$ when particles are meticulously placed one by one in an FCC or HCP arrangement. In this paper, particle permeability is defined as the likelihood of particles filling the void during the transition from RLP to RCP.

$$\frac{\rho_l}{\rho_c} = \frac{V_p + V_\varphi(1 - P_m)}{V_p + V_\varphi} \tag{11}$$

where ρ_c denotes the close packing density, ρ_l denotes the loose packing density, and P_m represents the mean particle permeability. Substituting Eq. 10 into Eq. 11, we get

$$P_m = \frac{(\rho_c - \rho_l)(V_p + V_\varphi)}{\rho_c V_\varphi} = \frac{\rho_c - \rho_l}{\rho_c(1 - \rho_l)} \tag{12}$$

At this point the particle permeability calculated from the packing density characterizes the permeability probability in all layers of particle stacks.

$$p_{i,j} = \frac{\rho_c^{i,j} - \rho_l^{i,j}}{\rho_c^{i,j}(1 - \rho_l^{i,j})} \tag{13}$$

To gauge the particle permeability, P_1, of the surface layer, it's beneficial to visualize each layer as an individualized, miniature particle stack. Intriguingly, as the size of the particles reduces, their aptitude to infiltrate subsequent layers amplifies. As these particles accrue, the consequent layer endures progressive compression from above, thereby augmenting the chance of populating the void spaces therein. This mechanism suggests a diminishing trend in particle permeability as we delve deeper into the internal layers of particles. In terms of stacking characteristics, the particles situated at the pinnacle are considered to be in the most lax configuration, while those anchored at the base manifest the most condensed state. Yet, this structure consistently aligns with the overall packing density, represented by p_c and p_l.

Due to $\rho_c = \frac{1}{Hk}\sum_i^H \sum_j^k \rho_c^{i,j}$, we assume that $\rho_c^{i,j} = f(i, j, \rho_c)$ is a linear function $(ai + bj + c = \rho_c^{i,j})$. The relationship between $\rho_c^{i,j}$ can be written as

$$\begin{aligned}\mathbb{P}_c &= \begin{bmatrix} \rho_c^{1,1} & \rho_c^{1,2} & \cdots & \rho_c^{1,k} \\ \rho_c^{2,1} & \rho_c^{2,2} & \cdots & \rho_c^{2,k} \\ \vdots & \vdots & \ddots & \vdots \\ \rho_c^{H,1} & \rho_c^{H,2} & \cdots & \rho_c^{H,k} \end{bmatrix} \\ &= \begin{bmatrix} \frac{1}{2}Hk(H+1) & \frac{1}{2}Hk(k+1) & Hk \end{bmatrix} \begin{bmatrix} a \\ b \\ c \end{bmatrix}\end{aligned} \tag{14}$$

where $\mathbb{P}_c$ is a $H \times k$ matrix. In addition, we let $\rho_c^{1,k} = \min(\mathbb{P}_c) = 0, \rho_c^{H,1} = \max(\mathbb{P}_c) = 2\rho_c < 1, c = 0$, and then we get $a = \frac{2\rho_c k}{Hk-1}, b = -\frac{a}{k}$. So, according to Eq. 13, the particle permeability $P_1 = [p_{1,1}, p_{1,2}, \ldots, p_{1,k}]$ for the surface layer can be written as

$$p_{1,j} = \frac{(\rho_c - \rho_l)(Hk - 1)}{\rho_c(Hk - 2\rho_l k - 2\rho_l j - 1)} \tag{15}$$

Assessing the packing density of particles is pivotal when determining their permeability. In this research, we've harnessed experimental data sourced from the EDEM simulation software to deduce particle packing density. The step-by-step methodology to estimate the overall PSD is delineated in Algorithm. 1.

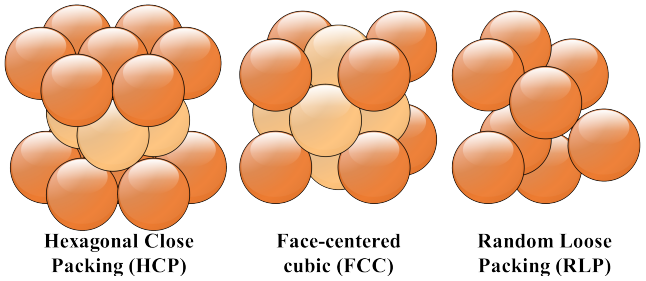

Figure 5. Different packing methods result in different packing densities. Both hexagonal close packing (HCP) and face-centered cubic (FCC) belong to random dense packing with a packing density of more than 0.74. The packing density of random loose packing (RLP) is about 0.60.

Algorithm 1 Estimating the overall PSD algorithm

Input: surface image I, depth image I_d, particle level k
Output: The overall PSD D_{total}

$D_1^{ac} \leftarrow f_D(f_{seg}(I))$
//Get the surface PSD from surface images.
$H \leftarrow I_d, d_m$
//Get the number of layers from depth images.
$P_1 \leftarrow H, k, \rho_c, \rho_l$
//Get the particle permeability from packing density.
$S_i \leftarrow r_i, l, \theta$
//Get the cross-section ratio for each layer
$D_{total} \leftarrow D_1^{ac}, H, P_1, S_i$
//Get the overall PSD

C. Surface Particle Size Detection Method based on Segmentation Model

1) Segmentation Model: Our approach to segmenting surface images and meticulously extracting particle contour

data was inspired by SAM [14]. Upon evaluation, we discerned that this model surpassed the semantic segmentation model in pinpointing particle contours: a crucial aspect for precise PSD computation. To bolster recognition precision, we trained the instance segmentation model using SAM and further honed it with labeled ore surface imagery.

2) Surface PSD: To yield accurate results, it's imperative to adopt a highly proficient method for particle size calculation, grounded on segmented imagery. Indeed, the technique chosen to detect individual particles critically influences the subsequent depiction of their PSD.

$$D_1^{ac} = f_D(f_{seg}(I)) \tag{16}$$

where f_D indicates the PSD calculation method, f_{seg} denotes the segmentation model, and I refers to the surface images. There exists a lot of methods to describe particle size, encompassing the triaxial diameter, projected diameter, spherical equivalent diameter, among others. It's noteworthy that the triaxial diameter approach is particularly adept for particles boasting a three-dimensional form. Conversely, the PSD method, underpinned by instance segmentation, gauges a particle's projected size along a specified axis. In this paper, we will be utilizing the projected diameter method. Projected diameters can be determined via a variety of techniques, such as Minimum Circle Diameter (MCD), Feret, Martin, and Heywood [29], [30]. The Heywood diameter, specifically, is delineated as the diameter of a circle that has the same area as the object's projected area. It can be calculated using the formula $d_H = \sqrt{\frac{4A}{\pi}}$, where A refers to the object's projected area [31].

It's important to note that particles positioned at an image's periphery are often incomplete and are hence termed as "edge particles." Given their lack of pixels, these particles can considerably skew the precision of particle size evaluations. Consequently, employing a universal calculation method for all particles becomes impractical [4]. To navigate this complexity, we adopted a strategy from existing literature that identifies whether a particle is situated at the edge. This method determines the edge location by checking if at least two contour points of a particle align with the image's boundary. For these edge particles, the Minimum Circle Diameter (MCD) was the chosen metric, while the Heywood diameter was deployed for complete particles. By harnessing this dual approach, we've been able to accurately compute the surface PSD via the instance segmentation-based detection technique.

In addition, the normalized mass distribution of the particles, denoted $M^n = [w_1, w_2, \ldots, w_k]$, is obtained from field acquisition, while the quantity distribution of the particles is obtained based on the segmented images, denoted $D = [n_1, n_2, ..., n_k]$. Therefore, we also need to establish a conversion relationship between these two.

$$w_k = \frac{m_k}{M} = \frac{n_k \bar{m}}{N \bar{m}} = \frac{n_k}{N} \tag{17}$$

where $\bar{m}$ refers to the mean mass of particle stacks, M indicates the total mass of particle stacks, N denotes the total quantity of particles, and n_k refers to the number of particles in the k-th particle level interval.

III. Experiment

A. Dataset and Experimental Platform

In our study, we specifically selected four prevalent types of ore particles commonly encountered on industrial conveyor belts: lump ore, coke, pellets, and sinter, as depicted in Fig. 6. From a consistently moving conveyor belt, we collected samples and procured surface images utilizing an industrial-grade camera [32]. Subsequently, these samples were processed through a multi-layer sieve, comprising between 3 to 9 layers. By weighing the results on a precise electronic scale, we were able to discern the PSD specific to each ore type. This methodology was diligently repeated over 100 times for each ore category present on the conveyor belt. Parallelly, throughout the sampling phase, we manually annotated the acquired surface images employing the Labelme annotation tool. These annotated images served a dual purpose: training and validating our surface image segmentation model, as well as testing its efficacy. By leveraging data augmentation strategies, we amassed a dataset consisting of 600 training samples, 100 validation samples, and an additional 100 samples reserved for testing: inclusive of the PSD data.

Our experiment utilized an impressive hardware configuration, including an Intel Core i9-9900K 3.6 GHz 32 GB and NVIDIA GeForce RTX2080TI 11 GB. The DEM process for the particle stack physical process was constructed at EDEM2018, while the instance segmentation model relied on a software environment featuring Python 3.7.6, PyTorch 1.4.0, CUDA 10.1, and CUDNN 7.6.5. For optimization, we relied on Adam with a learning rate of 1×10^{-4} and a cosine annealing learning rate scheduling policy to fine-tune the learning rate in the final epoch, with a minimum value of 1×10^{-6}. Additionally, weight decay was set to 1×10^{-8}.

B. Evaluation Metrics

1) PSD: Upon applying our proposed method, the end result manifests as the overall probability density function, rendered as a distribution. To validate the accuracy of this predicted distribution against its actual counterpart, we harness two distinct metrics: the Kullback-Leibler (KL) divergence and the Wasserstein distance (WD) [33]. The KL divergence stands as a commonly adopted metric to gauge the resemblance between two probability distributions. However, the WD presents a notable edge: it's adept at quantifying the proximity between two distributions, even when their respective support sets have limited or no overlap [34]. Given these characteristics, we strategically employ both the KL and WD metrics to rigorously evaluate the fidelity of our predicted distribution vis-à-vis the actual one.

$$\begin{aligned} KL &= \sum_{x \in X} A(x) \log \frac{A(x)}{B(x)} \\ WD(A, B) &= \inf_{\gamma \sim \prod(A,B)} E_{a,b \sim \gamma}(\|a - b\|) \end{aligned} \tag{18}$$

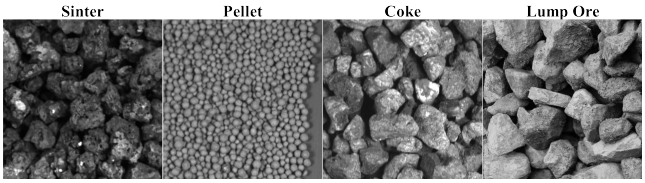

Figure 6. Some training images.

where A, B represent the two distributions, and $\prod(A, B)$ denotes the set of all possible joint distributions of the combination of distributions A and B. To facilitate the comparison of the variability of the results of different algorithms, we propose a composite distance metric with a value domain deflated to [0,100], denoted as $mDis = (e^{-\sqrt{KL}} + e^{-\sqrt{WD}})/2$.

2) Segmentation Model: Particle segmentation model's accuracy has a crucial impact on the calculated surface PSD. Hence, we evaluate the accuracy of our particle segmentation model using the most commonly used evaluation metric in the segmentation field today, which is mIoU (mean intersection over union). This evaluation metric is calculated as $mIoU = \frac{TP}{TP+FP+FN}$.

C. Comparison with the State-of-the-art PSD Detection Methods

1) Accuracy Comparison: In the course of our investigation, we conducted an exhaustive analysis of several advanced PSD detection techniques, encompassing ADPSD [35], CPSD [36], LUNet [15], RLPNet [4], MASU [20], MP [19], and SAM-psd (where SAM [14] serves as the foundational algorithm for surface PSD detection). ADPSD and CPSD are grounded in traditional segmentation-based paradigms, whereas LUNet and RLPNet adopt semantic segmentation techniques. In contrast, MASU R-CNN and MP implement instance segmentation to yield precise outcomes. The methodology we put forth demonstrated a marked superiority over contemporary, leading-edge PSD detection techniques, as corroborated by the KL, WD, and $mDis$ metrics delineated in Table. I. Our approach manifested a 2.49% enhancement in $mDis$ relative to SAM-psd, with a mere 0.81% augmentation in mIoU. Compared with methods singularly deploying the surface PSD for ultimate prediction, our technique leverages a mathematical model to infer the overall PSD from the surface PSD. This strategy partly accounts for the preeminence of our proposed method. Additionally, our findings underscored that the precision of the segmentation model profoundly influences the fidelity of PSD predictions. To bolster the segmentation precision for ore particle samples, we refined the pre-trained SAM model Vit-h using the ore particle dataset. This refinement culminated in a pronounced uptick in PSD computational accuracy, as depicted in Fig. 7, presenting outcomes for diverse test datasets.

2) Efficiency Comparison: The duration required for our methodology encompasses three pivotal phases: segmentation model inference, particle size determination, and comprehensive PSD computation. Our segmentation framework incorporates parameters analogous to SAM and maintains a parameter count consistent with Vit-h. In the testing phase, an image dimensioned at 2176*808 consumed roughly 10.8G of video memory on the 2080ti GPU. The computational procedures for determining particle size and the overarching PSD both possess time and space complexities of O(n), leading to expedited processing durations. As illustrated in Table. I, our approach attains an FPS marginally reduced by 0.01 in comparison to SAM-psd.

Table I
COMPARISON WITH THE LATEST PSD DETECTION METHODS

Method⋆	mIoU(↑)	KL(↓)	WD(↓)	mDis(↑)	FPS*
ADPSD [35]	73.41	0.411	0.027	68.70	0.67
CPSD [36]	72.84	0.422	0.029	68.29	0.83
LUNet [15]	77.63	0.365	0.022	70.39	**3.86**
RLPNet [4]	80.72	0.315	0.020	71.91	<u>2.72</u>
MASU [20]	82.39	0.245	0.019	73.99	1.64
MP [19]	81.17	0.276	0.020	72.95	1.95
SAM-psd [14]	<u>85.25</u>	<u>0.148</u>	**0.016**	<u>78.08</u>	0.20
Ours	**86.06**	**0.096**	<u>0.017</u>	**80.57**	0.19

*. The image size used for testing is 2176*808. We used sinter ([0,80]), coke ([0,80]), lump ore ([0,80]) and pellet ([0,20]) for testing.
⋆. The size of individual particles was calculated using Heywood method
(Bold: best; <u>Underline</u>: second best).

D. Comparative Validation under Different Parameters

The performance of our proposed method may be influenced by factors such as particle size range, morphology, hierarchical structure, permeability, and distribution ratios. It became imperative for us to validate the conceptual viability through visualization prior to undertaking meticulous comparative evaluations. Employing a virtual simulation via EDEM, grounded in authentic production data, emerges as a proficient means to realize this objective. By allocating distinct hues to silo particles depicted in the imagery, we can discern their respective descent durations, as elucidated in Fig. 8. For instance, particles denoted in blue might correspond to those descending within the inaugural second, those in yellow to the subsequent second, and so forth. Such a method facilitates a lucid comprehension of the stratified composition of the particle accumulation. Moreover, there exists a possibility that the packing density for certain specimens, like diverse ores, might diverge from historically recorded data. Consequently, the virtual simulation provided by EDEM becomes indispensable in ascertaining the most suitable packing density for each particular sample.

1) Different Particle Size Ranges: Through a comprehensive series of tests, we assessed the efficacy of our proposed approach on sinter exhibiting diverse particle size intervals: [0mm, 20mm], [40mm, 80mm], and [0mm, 80mm], as delineated in the initial three rows of Table. II. Intriguingly, the outcomes revealed a performance hierarchy that was counterintuitive: poorest for the [0, 20] range, intermediate for [40, 80], and optimal for [0, 80], even when the particle permeability metrics remained consistent (ρ_c=0.69, ρ_l=0.60,

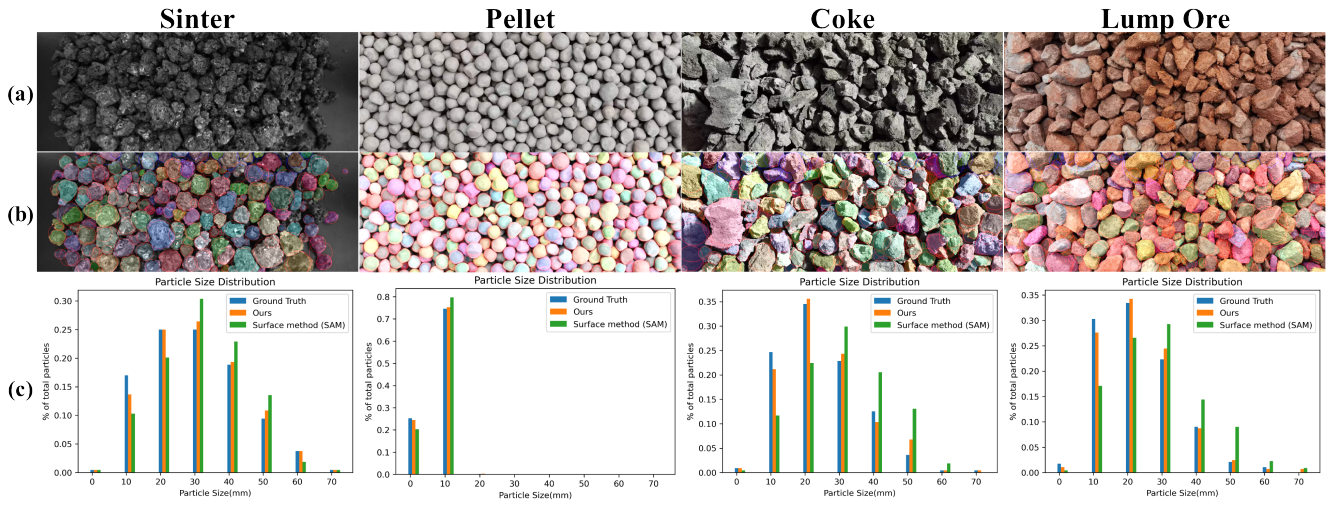

Figure 7. Experimental results for some test samples. (a) surface images; (b) Segmentation results and particle size calculations obtained by our method. The red and blue circles in the figure indicate calculations for individual particle sizes.(c) Calculation of overall PSD. The PSDs in the graphs are all normalized. The average weights of sinter ([0,80]), pellet ([0,20]), coke ([0,80]), and lump ore ([0,80]) in the figure are 295 g, 31 g, 54 g, and 267 g, respectively. According to the accuracy of surface image segmentation, pellet displays the highest precision, followed by lump ore and coke. Conversely, sinter exhibits the lowest accuracy due to its complex edge shape. Moreover, the simple edge shape of pellet proves advantageous in calculating the size of individual particles, ultimately leading to a more precise PSD.

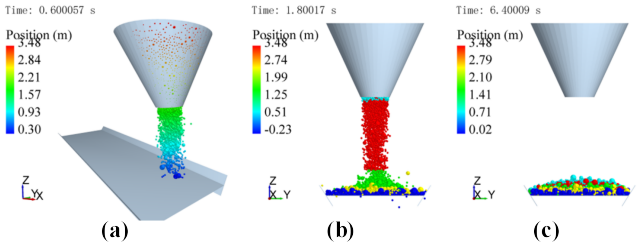

Figure 8. Simulation of particle accumulation process. (a) Stereoscopic view at the beginning of the simulation; (b) in simulation (different colored particles indicate results of random sampling at different T moments). (c) Particle stack stationary (Although some particles can penetrate the lower layers, the stratification of the particle stack is still noticeable). The packing density was determined by calculating the particle and void volume at rest.

Table II
COMPARISON AT DIFFERENT PARTICLE SIZE RANGES/PROPORTIONS

PSD	size ranges	Ours*		SAM-psd
		$p_{1,1}$=0.205	$p_{1,1}$=0.150	
[0.28, 0.72, 0.00, 0.00, 0.00, 0.00, 0.00, 0.00]	[0, 20]	78.99	79.38	78.50
[0.00, 0.00, 0.00, 0.00, 0.37, 0.29, 0.23, 0.11]	[40, 80]	79.35	80.11	79.33
[0.16, 0.34, 0.18, 0.12, 0.10, 0.06, 0.03, 0.01]	[0, 80]	79.24	79.49	77.92
[0.02, 0.03, 0.05, 0.10, 0.11, 0.20, 0.35, 0.14]	[0, 80]	79.93	**80.62**	78.45
[0.02, 0.08, 0.22, 0.30, 0.16, 0.12, 0.06, 0.04]	[0, 80]	**80.51**	79.20	78.31

*. Here, we use the untuned SAM pre-trained model to recognize the sinter. We default the HPM to a three-layer structure and $p_{1,1} = 0.205$.

and $p_{1,1}$=0.205 as per Eq. (15)). Delving deeper into these results, it became apparent that the dimensions of the smaller particles significantly exceeded the interstices among their larger counterparts, leading to diminished particle permeability, which in turn impeded the method's performance. To address this discrepancy, we adjusted the particle permeability values to (ρ_c=0.65, ρ_l=0.59, and $p_{1,1}$=0.150) and re-evaluated the method's efficacy. As anticipated, the subsequent results unveiled a marked enhancement in performance for the [0, 20] and [40, 80] ranges, attributed to the revised particle permeability metrics more congruently reflecting the truth.

2) Different Proportions of Particles with the Same Size Ranges: In our systematic experimentation, we assessed varying proportions of sinter, curated by sieving, with particle dimensions segmented into eight categories spanning from 0 to 80. The first group consisted mostly of small particles, the second mostly of large particles, and the third was more homogeneous with PSDs resembling a log-normal distribution, as shown in the last three rows of Table. II. The experimental results showed that the proposed method performed best in the third group, moderately in the first group, and worse in the second group. We repeated the experiment with reduced particle permeability and found that the proposed method improved performance in the first and second groups, but decreased performance in the third group. This is likely due to the fact that particles in the first and second groups are relatively similar in size, making it difficult for particle penetration to occur. The smaller the particle size difference, the more challenging it is for particles to penetrate.

3) Different Particle Size Partitioning: Table. III presents the performance metrics of the proposed technique across diverse particle size partitioning, encompassing k=4, k=8 (the default configuration for most experiments), and k=10. The data underscores HPM's consistent superiority over

Table III
COMPARISON OF METHODS AT DIFFERENT PARTICLE SIZE INTERVALS

Number of intervals $k^\star$	Mehtod*	KL(↓)	WD(↓)	mDis(↑)
4	SAM-psd	0.068	0.027	81.00
	Ours	0.056	0.033	81.19
8	SAM-psd	0.148	0.016	78.08
	Ours	0.112	0.016	79.84
10	SAM-psd	0.111	0.009	81.34
	Ours	0.097	0.009	82.15

*. Here, we use the untuned SAM pre-trained model Vit-h to recognize sinter ([0,80]). We default the HPM to a three-layer structure with $p_{1,1} = 0.205$.
$\star$. If a different number of intervals k is used, the number of sieve layers required varies (if k=4, only a 3-layer sieve is required).

Table IV
COMPARISON OF METHODS WITH DIFFERENT NUMBER OF LAYERS

Number of layers H	Mehtod*	KL(↓)	WD(↓)	mDis(↑)
-	SAM-psd	0.148	0.016	78.08
2	Ours	0.129	0.016	78.96
3	Ours	0.112	**0.016**	79.84
4	Ours	**0.082**	0.018	**81.21**

*. Here, we use the untuned SAM pre-trained model Vit-h to recognize sinter ([0,80]). We default $k = 8$ and $p_{1,1} = 0.205$.

SAM-psd. It's imperative to recognize that the performance of the proposed approach is susceptible to variations in particle size partitioning. Employing fewer partitions may render the PSD less discerning, thereby limiting its industrial applicability due to increased ambiguity. Conversely, opting for a partitioning of k=10, which necessitates nine sieve layers, might yield superfluous data, especially if certain intervals lack particles. Moreover, as the granularity of the particle size partitioning escalates, the model's estimation precision becomes increasingly vulnerable to computational discrepancies. Notably, the same particle could be classified under divergent size intervals, contingent on the particle size computation methodology, culminating in excessive PSD categorization. Nevertheless, such over-segmentation doesn't inherently compromise predictive precision. In deducing the holistic PSD, it is judicious to adopt either 4 or 8 dimensions, streamlining the process and potentially augmenting model accuracy. However, if the predicted PSD is only one dimensional, its estimation complexity is equated to crowd density evaluation, which predicates merely the particle count.

4) Different Number of Stacked Layers: Table. IV showcases the outcomes when our methodology is employed on stacks comprising 2, 3, and 4 layers. The layer count can be ascertained by substituting d_m with the average value derived from the detected surface PSD. The value of h emerges from the depth disparity within the particle stack's surface layer. To bolster the credibility of our computations, we analyzed multiple samples across time rather than placing undue reliance on a singular sample's outcome. The HPM results affirm that our technique outperforms segmentation-focused surface detection approaches across stacks of diverse layer quantities, underscoring the accuracy of the proposed HPM.

Table V
KRUSKAL-WALLIS ANOVA TABLE

Source*	SS	df	MS	Chi-sq	Prob>Chi-sq (P)
Groups*	0.563	1	0.5625	0.02	0.8747
Error	338.938	14	24.2098	-	-
Total	339.5	15	-	-	-

*. Here, we use the tuned SAM model to recognize sinter ([0,80]). We default $k = 8$ and $p_{1,1} = 0.205$.
$\star$. Groups: the array obtained by splicing the predicted PSDs and truth values, i.e., the input; SS: the sum of the squares of the predicted PSD and the true value; df: Degrees of freedom, i.e., df = m-1 (m denotes the number of data sets involved in the detection, here the only two sets involved in the detection are our predicted PSDs and truth values); MS: the mean squares of the predicted PSD and the true value; Chi-sq: the chi-square statistic of the predicted PSD and the true value; Prob>Chi-sq: p-value, a measure for testing whether there is a significant difference between multiple distributions (predicted PSD vs. true value).

5) Different Particle Shapes: Particle shape analysis is a multifaceted subject demanding thorough scrutiny and contemplation. We embarked on experiments with four diverse ore types: sinter (irregular), pellet (spherical), coke (irregular), and lump ore (irregular), with the corresponding outcomes illustrated in Fig. 7. The $mDis$ results for the four ores stand at: sinter (80.16), pellet (81.02), coke (79.74), and lump ore (79.25). Our analysis reveals that the commendable precision observed for pellets can be ascribed to their impeccably segmented surfaces, compounded by the advantages of their inherent spherical geometry. In contrast, sinter, despite its overall spherical semblance, encompasses a larger cumulative void volume, manifested through more pronounced concavities and diminished packing density, and exhibits a natural stacking inclination, characterized by a rougher surface and heightened friction. These attributes facilitate the penetration of minuscule particles into the underlying strata, rendering the HPM estimates more congruent with the real-world scenario. Both coke and lump ore, typically having an extended morphology, are predisposed to cast shadows on their surface, which subsequently influences the calculation of individual particle dimensions and surface PSD.

Additionally, the diversity in particle shapes can impact the estimation of individual particle dimensions and the corresponding surface PSD. It is crucial to acknowledge that computations utilizing the projected diameter formula might introduce minor discrepancies. Nonetheless, an undue focus on the results of singular particle size estimations while determining the PSD is unwarranted. This is predicated on the understanding that the deduced PSD serves as a statistical metric, encapsulating the aggregate physical attributes of the particle ensemble. Given an ample sample size, minor deviations in ascertaining an individual particle's size diminish in significance. Consequently, many scholars delving into particle materials often resort to a perfect sphere as a model in simulations to streamline their calculations.

6) Significance Test: To evaluate the precision of the overall PSD derived using our proposed method, we instituted a significance test on the estimation outcomes. However, the PSD data deviates from a normal distribution,

contravening the foundational prerequisites of parametric ANOVA (Analysis of Variance). In response to this challenge, we adopted the Kruskal-Wallis test, a renowned nonparametric method, for our data analysis [37]. The results from the Kruskal-Wallis test substantiate that there isn't a notable discrepancy between the forecasted PSD and its true value, as delineated in Table. V. This assertion is further corroborated by the computed p-value of 0.8747, exceeding the significance threshold of 0.05. From this, we deduce that the anticipated PSD conforms to fundamental statistical principles.

E. Limitations

1) Geometric Model: While our method has demonstrated commendable performance relative to contemporary state-of-the-art PSD detection techniques, it isn't devoid of limitations. One primary constraint revolves around the accurate modeling of particle and stack geometries. In particular, we've predicated our model on the assumptions that particle stacks are essentially nested, multi-layered cylindrical structures and that individual particles are spherical in nature. Although this assumption is widely favored by particle material researchers for its simplicity, it could be a source of potential inaccuracies [38]–[40]. Nevertheless, our proposed framework showcases adaptability to particles across a spectrum of sizes. Its performance would further benefit from more precise sensors dedicated to surface PSD detection. While this framework holds promise for extensions into other types of stacks, it mandates tailored adjustments to ensure the optimal spatial modeling of the respective particle stacks.

2) Hierarchical Division: In our exploration of particle stack stratification, we've anchored our methodology on certain assumptions, especially in aspects like determining each layer's height and the number of stratification layers. Though these assumptions might introduce a measure of bias, their influence on the final output is marginal. Importantly, as we increase the sample size, the impact of these assumptions will decrease, effectively curbing bias. Moving forward, exploring more effective approaches for determining the each layer height and the number of delaminations could enhance the accuracy of our methodology.

IV. CONCLUSION

Our research introduces a novel hierarchical packing model designed to precisely estimate the overall PSD within a particle stack. Central to this model is the inherent interplay between particle penetration, spatial distribution, and packing density. By leveraging these correlations, we've managed to construct the mathematical relationship between surface and overall PSD, subsequently enhancing the estimation accuracy of the latter. However, it's worth highlighting that variables like particle shape, size, and definition each carry distinct impacts on particle permeability, which, in turn, influence the efficacy of our proposed method. The assumptions underpinning the hierarchical packing model, like the number of layers, individual layer height, and stack shape, also bear on the outcomes. Looking ahead, our research ambitions are trained on a deeper foray into particle dynamics. We hope to unpack the intricacies of particle infiltration and thereby gain a richer understanding of the particle stack formation narrative.

REFERENCES

[1] F. Caputo, J. Clogston, L. Calzolai, M. Rösslein, and A. Prina-Mello, "Measuring particle size distribution of nanoparticle enabled medicinal products, the joint view of euncl and nci-ncl. a step by step approach combining orthogonal measurements with increasing complexity," *Journal of Controlled Release*, vol. 299, pp. 31–43, 2019.

[2] Y.-J. Mao, S. J. Barnes, J. Duan, K.-Z. Qin, B. M. Godel, and J. Jiao, "Morphology and particle size distribution of olivines and sulphides in the jinchuan ni–cu sulphide deposit: evidence for sulphide percolation in a crystal mush," *Journal of Petrology*, vol. 59, no. 9, pp. 1701–1730, 2018.

[3] F. Yu, Q. Wang, Q. Yan, N. Jiang, J. Wei, Z. Wei, and S. Yin, "Particle size distribution, chemical composition and meteorological factor analysis: A case study during wintertime snow cover in zhengzhou, china," *Atmospheric Research*, vol. 202, pp. 140–147, 2018.

[4] J. Liu, Z. Jiang, W. Gui, and Z. Chen, "A novel particle size detection system based on rgb-laser fusion segmentation with feature dual-recalibration for blast furnace materials," *IEEE Transactions on Industrial Electronics*, vol. 70, no. 10, pp. 10 690–10 699, 2022.

[5] Z. Jiang, J. Yu, J. Liu, Z. Chen, W. Gui, and T. Cao, "A coke detection method based on reweighting a composite feature for mixed material recognition and quantification," *IEEE TRANSACTIONS ON INSTRUMENTATION AND MEASUREMENT*, vol. 71, p. 5024512, 2022.

[6] L. He, Z. Jiang, Y. Xie, W. Gui, and Z. Chen, "Mass flow measurement of molten iron from blast furnace, based on trusted region stacking using single high-speed camera," *IEEE Transactions on Instrumentation and Measurement*, vol. 70, 2021.

[7] Y. Fang, Z. Jiang, D. Pan, W. Gui, and Z. Chen, "Soft sensors based on adaptive stacked polymorphic model for silicon content prediction in ironmaking process," *IEEE Transactions on Instrumentation and Measurement*, vol. 70, pp. 1–12, 2021.

[8] J. Zhu, W. Gui, Z. Chen, and Z. Jiang, "A novel non-contact and real-time blast furnace stockline detection method based on burden surface video streams," *IEEE Transactions on Instrumentation and Measurement*, vol. 72, pp. 1–13, 2023.

[9] C. Igathinathane, U. Ulusoy, and L. Pordesimo, "Comparison of particle size distribution of celestite mineral by machine vision σvolume approach and mechanical sieving," *Powder Technology*, vol. 215, pp. 137–146, 2012.

[10] J. P. Schwarz, R. Gao, D. Fahey, D. Thomson, L. Watts, J. Wilson, J. Reeves, M. Darbeheshti, D. Baumgardner, G. Kok *et al.*, "Single-particle measurements of midlatitude black carbon and light-scattering aerosols from the boundary layer to the lower stratosphere," *Journal of Geophysical Research: Atmospheres*, vol. 111, no. D16, 2006.

[11] L. Zhang and J. Kulon, "Comparative study of square and sine-wave excitation methods for the measurement of aerosol particles charge and size distribution using phase doppler anemometry," *IEEE Transactions on Instrumentation and Measurement*, vol. 60, no. 4, pp. 1397–1407, 2011.

[12] R. J. Bomphrey, N. J. Lawson, N. J. Harding, G. K. Taylor, and A. L. Thomas, "The aerodynamics of manduca sexta: digital particle image velocimetry analysis of the leading-edge vortex," *Journal of Experimental Biology*, vol. 208, no. 6, pp. 1079–1094, 2005.

[13] J. Liu, Z. Jiang, T. Cao, Z. Chen, C. Zhang, and W. Gui, "Generated pseudo-labels guided by background skeletons for overcoming under-segmentation in overlapping particle objects," *IEEE Transactions on Circuits and Systems for Video Technology*, 2022.

[14] A. Kirillov, E. Mintun, N. Ravi, H. Mao, C. Rolland, L. Gustafson, T. Xiao, S. Whitehead, A. C. Berg, W.-Y. Lo *et al.*, "Segment anything," *arXiv preprint arXiv:2304.02643*, 2023.

[15] J. Duan, X. Liu, X. Wu, and C. Mao, "Detection and segmentation of iron ore green pellets in images using lightweight u-net deep learning network," *Neural Computing and Applications*, vol. 32, pp. 5775–5790, 2020.

[16] Z. Wang, D. Li, X. Zheng, and D. Xie, "A novel coal dust characteristic extraction to enable particle size analysis," *IEEE Transactions on Instrumentation and Measurement*, vol. 70, pp. 1–12, 2021.

[17] A. Singh, H. Kalke, M. Loewen, and N. Ray, "River ice segmentation with deep learning," *IEEE Transactions on Geoscience and Remote Sensing*, vol. 58, no. 11, pp. 7570–7579, 2020.

[18] W. Liu, X. Yang, X. Yang, and H. Gao, "A novel industrial chip parameters identification method based on cascaded region segmentation for surface-mount equipment," *IEEE Transactions on Industrial Electronics*, vol. 69, no. 5, pp. 5247–5256, 2022.

[19] R. Cohn, I. Anderson, T. Prost, J. Tiarks, E. White, and E. Holm, "Instance segmentation for direct measurements of satellites in metal powders and automated microstructural characterization from image data," *Jom*, vol. 73, no. 7, pp. 2159–2172, 2021.

[20] P. Monchot, L. Coquelin, K. Guerroudj, N. Feltin, A. Delvallée, L. Crouzier, and N. Fischer, "Deep learning based instance segmentation of titanium dioxide particles in the form of agglomerates in scanning electron microscopy," *Nanomaterials*, vol. 11, no. 4, p. 968, 2021.

[21] M. Li, X. Wang, H. Yao, H. Saxén, and Y. Yu, "Analysis of particle size distribution of coke on blast furnace belt using object detection," *Processes*, vol. 10, no. 10, p. 1902, 2022.

[22] G. Chebil, D. Bettebghor, Y. Renollet, P. Lapouge, C. Davoine, M. Thomas, V. Favier, and M. Schneider, "Deep learning object detection for optical monitoring of spatters in l-pbf," *Journal of Materials Processing Technology*, vol. 319, p. 118063, 2023.

[23] O. Oreifej, X. Li, and M. Shah, "Simultaneous video stabilization and moving object detection in turbulence," *IEEE transactions on pattern analysis and machine intelligence*, vol. 35, no. 2, pp. 450–462, 2012.

[24] C. C. Furnas, "The relations between specific volume, voids, and size composition in systems of broken solids of mixed sized, department of commerce, bureau of mines," *Reports of investigations*, pp. 1–10, 1928.

[25] A. R. Westman and H. Hugill, "The packing of particles 1," *Journal of the American Ceramic Society*, vol. 13, no. 10, pp. 767–779, 1930.

[26] J.-H. Kim, K.-W. On, W. Lim, J. Kim, J.-W. Ha, and B.-T. Zhang, "Hadamard product for low-rank bilinear pooling," *arXiv preprint arXiv:1610.04325*, 2016.

[27] J. Kepler, *The six-cornered snowflake*. Paul Dry Books, 2010.

[28] Q. Qian, X. An, Y. Wang, Y. Wu, and L. Wang, "Physical study on the vibrated packing densification of mono-sized cylindrical particles," *Particuology*, vol. 29, pp. 120–125, 2016.

[29] Y. Wu, G. Castle, and I. Inculet, "Particle size analysis in the study of induction charging of granular materials," *Journal of Electrostatics*, vol. 63, no. 3, pp. 189–202, 2005, selected Papers from the ESA 2004 Annual Conference.

[30] T. Church, "Problems associated with the use of the ratio of martin's diameter to feret's diameter as a profile shape factor," *Powder Technology*, vol. 2, no. 1, pp. 27–31, 1968.

[31] T. F. Guimarães, A. D. Lanchote, J. S. da Costa, A. L. Viçosa, and L. A. P. de Freitas, "A multivariate approach applied to quality on particle engineering of spray-dried mannitol," *Advanced Powder Technology*, vol. 26, no. 4, pp. 1094–1101, 2015.

[32] Z. Yi, Z. Jiang, J. Huang, X. Chen, and W. Gui, "Optimization method of the installation direction of industrial endoscopes for increasing the imaged burden surface area in blast furnaces," *IEEE Transactions on Industrial Informatics*, vol. 18, no. 11, pp. 7729–7740, 2022.

[33] J. Goldberger, S. Gordon, H. Greenspan *et al.*, "An efficient image similarity measure based on approximations of kl-divergence between two gaussian mixtures." in *ICCV*, vol. 3, 2003, pp. 487–493.

[34] S. Singh and B. Póczos, "Minimax distribution estimation in wasserstein distance," *arXiv preprint arXiv:1802.08855*, 2018.

[35] Y. Meng, Z. Zhang, H. Yin, and T. Ma, "Automatic detection of particle size distribution by image analysis based on local adaptive canny edge detection and modified circular hough transform," *Micron*, vol. 106, pp. 34–41, 2018.

[36] Z. Zhang, J. Yang, L. Ding, and Y. Zhao, "Estimation of coal particle size distribution by image segmentation," *International Journal of Mining Science and Technology*, vol. 22, no. 5, pp. 739–744, 2012.

[37] P. E. McKight and J. Najab, "Kruskal-wallis test," *The corsini encyclopedia of psychology*, pp. 1–1, 2010.

[38] A. Averardi, C. Cola, S. E. Zeltmann, and N. Gupta, "Effect of particle size distribution on the packing of powder beds: A critical discussion relevant to additive manufacturing," *Materials today communications*, vol. 24, p. 100964, 2020.

[39] S. Chu, J. Chen, L. Li, P. Ng, and A. Kwan, "Roles of packing density and slurry film thickness in synergistic effects of metakaolin and silica fume," *Powder Technology*, vol. 387, pp. 575–583, 2021.

[40] G. Fu and W. Dekelbab, "3-d random packing of polydisperse particles and concrete aggregate grading," *Powder technology*, vol. 133, no. 1-3, pp. 147–155, 2003.